Geomorphology 383 (2021) 107683

Contents lists available at ScienceDirect

Geomorphology

journal homepage: www.elsevier.com/locate/geomorph

Monitoring terrain elevation of intertidal wetlands by utilising the spatial-temporal fusion of multi-source satellite data: A case study in the Yangtze (Changjiang) Estuary

Wenli Gao [a], Fang Shen [a,b,*], Kai Tan [a], Weiguo Zhang [a], Quanxing Liu [a], Nina S.N. Lam [c], Jianzhong Ge [a]

[a] State Key Laboratory of Estuarine and Coastal Research, East China Normal University, Shanghai 200241, China
[b] Institute of Eco-Chongming (IEC), Shanghai 200062, China
[c] Department of Environmental Sciences, Louisiana State University, Baton Rouge, LA 70803, USA

ARTICLE INFO

Article history:
Received 25 September 2020
Received in revised form 28 February 2021
Accepted 1 March 2021
Available online 5 March 2021

Keywords:
Terrain elevation
Intertidal wetland
Remote sensing
Spatial-temporal data fusion
Yangtze (Changjiang) Estuary

ABSTRACT

Intertidal wetlands are dynamic geomorphological areas located at the land-sea interface and perform multiple ecosystem functions. Owing to increased human activities, intertidal wetlands have been subjected to dramatic changes in recent decades; therefore, high-resolution monitoring of wetland topography is critical to its management. However, satellite imagery with high spatial resolution usually demonstrates a low revisit frequency (e.g. several days to greater than ten days) and is frequently obstructed by clouds, limiting its capability to display the high-resolution time-series information of intertidal wetland terrain elevation variations. Conversely, satellite imagery with a high revisit frequency generally demonstrates a lower spatial resolution. In this study, a spatial-temporal data fusion method was utilised to generate hourly time-series images with a spatial resolution of 16 m by combining the satellite GF-1/WFV data (spatial resolution: 16 m; revisit frequency: 4 days) with geostationary satellite GOCI data (spatial resolution: 500 m; revisit frequency: 1 h). In combination with the tidal level information, digital terrain elevation (DTM) data of the intertidal wetland can be derived from fusion images. The DTM was synchronously validated by the terrain elevation data acquired on the same day utilising unmanned aerial vehicle (UAV)-borne LiDAR in the North Branch intertidal wetland of Chongming Island, Yangtze Estuary, with a root mean square error of 0.16 m. The application in Chongming-Dongtan indicates that this method is effective for monitoring high dynamic changes in intertidal wetland terrain elevations.

1. Introduction

Intertidal wetlands, which are sensitive transition zones located between the land and sea, are one of the most vulnerable ecosystems on the planet and possess significant economic and research value (Kirwan and Megonigal, 2013). Owing to increasing human activities and climate change, intertidal wetlands have undergone rapid changes over recent decades worldwide; therefore, monitoring intertidal wetland terrain elevations with high spatial-temporal resolution and reasonable vertical accuracy is essential for a better understanding of coastal system evolution and management (Benveniste et al., 2019). Traditional surveying techniques (e.g. levelling, robotic total station, and real-time kinematic) can provide extremely accurate terrain elevation measurements (Mason et al., 2000); however, these techniques are time-consuming, labourious, and inefficient in terms of spatial coverage. Furthermore, periodic flooding, dense vegetation coverage, and muddy environments often render intertidal wetlands inaccessible for execution of in-situ studies (Tan et al., 2020). As such, conventional methods cannot be used effectively to obtain intertidal wetland terrain elevation data over a wide area (Mason et al., 2000; Choi and Kim, 2018). Therefore, the acquisition of intertidal wetland topography and geomorphological data is challenging.

Satellite remote sensing techniques can provide synchronous observations over large areas with advantages of short-period revisit, low costs, and non-contact measurements, providing an effective method to study dynamic changes in intertidal wetlands (Ryu et al., 2002; Liu et al., 2013b; Salameh et al., 2019). Currently, intertidal wetland topography obtained via remote sensing techniques can be constructed mainly by the following four methods: the waterline detection method (WDM) (Mason et al., 1995; Shen et al., 2008), the analysis of satellite stereo image pairs (Tateishi and Akutsu, 1992; Almeida et al., 2019), the analysis of interferometric synthetic aperture radar (Lee and Ryu, 2017; Choi and Kim, 2018), and satellite radar altimetry (Salameh et al., 2018).

Among these methods, the WDM is the most widely utilised technique for constructing the intertidal wetland digital terrain elevations

* Corresponding author at: State Key Laboratory of Estuarine and Coastal Research, East China Normal University, Shanghai 200241, China.
E-mail address: fshen@sklec.ecnu.edu.cn (F. Shen).

https://doi.org/10.1016/j.geomorph.2021.107683
0169-555X/

using non-stereo remote sensing imagery. This is because optical images are more abundant and easily obtained than stereoscopic images and radar data. WDM implementation methods mainly include visual interpretation, threshold segmentation, and edge detection. The visual interpretation method is highly accurate but requires a considerable amount of work. The threshold segmentation method involves the commonly utilised Normalized Difference Water Index (NDWI) (Mcfeeters, 1996). The method is simple, fast, and effective for waterline extractions of clear water and sandy coasts, as the clear water exhibits strong absorption characteristics beyond 600 nm and absorbs the majority of the incident solar radiation in the near-infrared and short-wave infrared bands, with little reflected radiation. However, for muddy water and tidal flats, the threshold segmentation method is not suitable due to the high reflectance of turbid waters in the visible to near-infrared bands of satellite imagery (Shen et al., 2008). Edge detection methods, including the Sobel, Canny, and Roberts operators, have been used to extract the waterline in muddy tidal wetlands; however, they are influenced by noise arising from the imagery. To improve waterline extraction accuracy, this study adopted a repeatable and verifiable method based on the backpropagation (BP) neural network approach (Tochamnanvit and Muttitanon, 2014) to extract the waterline. This method is a type of supervised classification with high accuracy owing to its use of a variety of time-series training samples. The extracted waterline is regarded as a type of 'contour line', and due to the dynamic changes of the waterline, a series of waterline contours are utilised and combined to construct the intertidal wetland terrain elevation.

To minimise waterline extraction errors caused by the impact of the spatial resolution of the satellite imagery, high spatial resolution images, such as Landsat TM/ETM/OLI, Worldview-2, SPOT-1/2 and etc., have often been utilised (Anthony et al., 2008; He and Wu, 2008; Shen et al., 2008; Ghosh et al., 2015; Purkis et al., 2016). To reduce the influence of intertidal wetland changes on terrain elevation, Liu et al. (2012) employed the WDM for waterline extraction and generated a series of waterline contours from satellite images over a one-year period. Khan et al. (2019) combined tidal level data and Sentinel-2/MSI images with a spatial resolution of 10 m to extract a series of waterline contours and constructed the digital terrain elevation of the Bengal Delta from satellite images acquired over a period spanning three years. However, studies have found that if an intertidal wetland DTM is constructed by extracting a series of waterline contours from satellite images acquired over several years, the satellite images utilised to construct the DTM may have a large bias and it is hard to detect the interannual dynamic change of the elevation (Ryu et al., 2008; Zhao et al., 2008). To simultaneously satisfy the need for temporal and spatial resolutions, a digital terrain elevation construction method based on MODIS images was proposed by Liu et al. (2013a). This method integrated the water edge points generated by multiple satellite images to obtain a three-month time interval. Kang et al. (2017) selected Landsat TM/OLI and HJ-1A/B CCD images obtained over a period of five months, to map the DTM over the northern Jiangsu Shallow Bank. The accuracy of terrain elevation has been improved to some extent by reducing the time span, but it was still far from enough for the intertidal wetland with rapid dynamic changes.

Generally, for remote sensing techniques, there is a technical trade-off between the spatial and temporal resolutions of remote sensing images obtained by a single satellite sensor. To resolve this, this study proposed a new approach to derive the DTM of intertidal wetlands in the Yangtze Estuary by considering multi-source satellite data fusion. A spatial and temporal adaptive reflectance fusion model (STARFM) (Gao et al., 2006) was adopted to generate hourly imagery with a spatial resolution of 16 m, by data fusion of polar-orbiting satellite GF-1/WFV (spatial resolution: 16 m; revisit frequency: 4 days) and GOCI satellite (spatial resolution: 500 m; revisit frequency: 1 h) data. In combination with the tidal level data, the terrain elevation measurement errors caused by tidal phase differences in the Yangtze Estuary were markedly reduced, and the muddy tidal wetlands and water bodies were accurately classified based on the neural network supervised classification method. Compared with existing methods, the advantages of this proposed method are that the time interval is reduced to 1 h and the spatial resolution is 16 m, which benefits the monitoring of dynamic intertidal wetland terrain elevations significantly. The validation dataset utilised in this study was acquired by using an UAV-borne LiDAR because the LiDAR technology demonstrates the advantages of high speed, flexibility, and accuracy in topographic mapping (Irish and White, 1998; Wehr and Lohr, 1999). The purpose of this study was to improve the accuracy of intertidal wetland terrain elevation by utilising multi-source satellite spatial-temporal fusion, so as to achieve efficient, accurate terrain elevation data extraction.

2. Study area and datasets

2.1. Study area

The Yangtze Estuary (Fig. 1) is one of the largest estuaries in the world in terms of river discharge (Shen et al., 2013) and the abundant sediment loads from the Yangtze River have resulted in extensive tidal wetlands development (Chen et al., 1979). The sediments have formed vast and developed intertidal wetlands, sand bars, side beaches, and other landforms, resulting in the formation of a complex topography of the intertidal wetlands in the Yangtze Estuary (Li et al., 2016). The wetland area of the Yangtze Estuary is approximately 4725 km^2 (Sun et al., 2018), the average tidal range near the mouth of the Yangtze Estuary is approximately 2.7 m, and the maximum tidal range during spring tide is 5 m (Chen et al., 1988).

The Yangtze Estuary is divided into the North and South Branch by Chongming Island. The North Branch is a shallow, funnel-type channel, resulting in a net landward transport of sediment and channel siltation. Owing to the Coriolis force, the southern bank of the North Branch accumulates sediments faster and the coastline progrades rapidly.

This study focused on the southern bank of the North Branch, located between 121°36′E–121°52′E and 31°35′N–31°43′N, with an approximate area of 23 km^2.

2.2. GF-1/WFV and GOCI satellite data

Owing to the need for acquisition of high spatial- and temporal-resolution images over the study area, polar-orbiting high spatial resolution satellite GF-1/WFV data with 16 m spatial and 4 days temporal resolutions (Bai, 2013) and GOCI satellite data with 500 m spatial and 1 h temporal resolutions (Si and Ying, 2010) were selected as data sources. Compared with the Landsat-8/OLI data, the GF-1/WFV data have higher spatial resolution, revisit frequency and a wider swatch width of the image (Shang and Shen, 2016). GF-1/WFV data products can be obtained without incurred costs from the China Centre for Resources Satellite Data and Application (http://www.cresda.com). GOCI level-1 radiance data were provided by the Korea Ocean Satellite Centre (http://kosc.kiost.ac.kr), and the level-2 data with radiometric and geometric corrections were obtained after processing the level-1 data using the ground data processing system (http://kosc.kiost.ac.kr/eng/p30/kosc_p34.html). In this study, 12 remote sensing images were utilised, including 7 GF-1/WFV images across the whole year 2019 and 5 GOCI images collected on 17 August 2019.

2.3. Tide-gauge station data

The closest tide-gauge station to the study area was located at Lianxing port (denoted by the yellow star in Fig. 1a); therefore, the tidal level data from this station were utilised in this study. Table 1 shows the tidal level data measured from the Lianxing port tide-gauge station at the corresponding satellite image time.

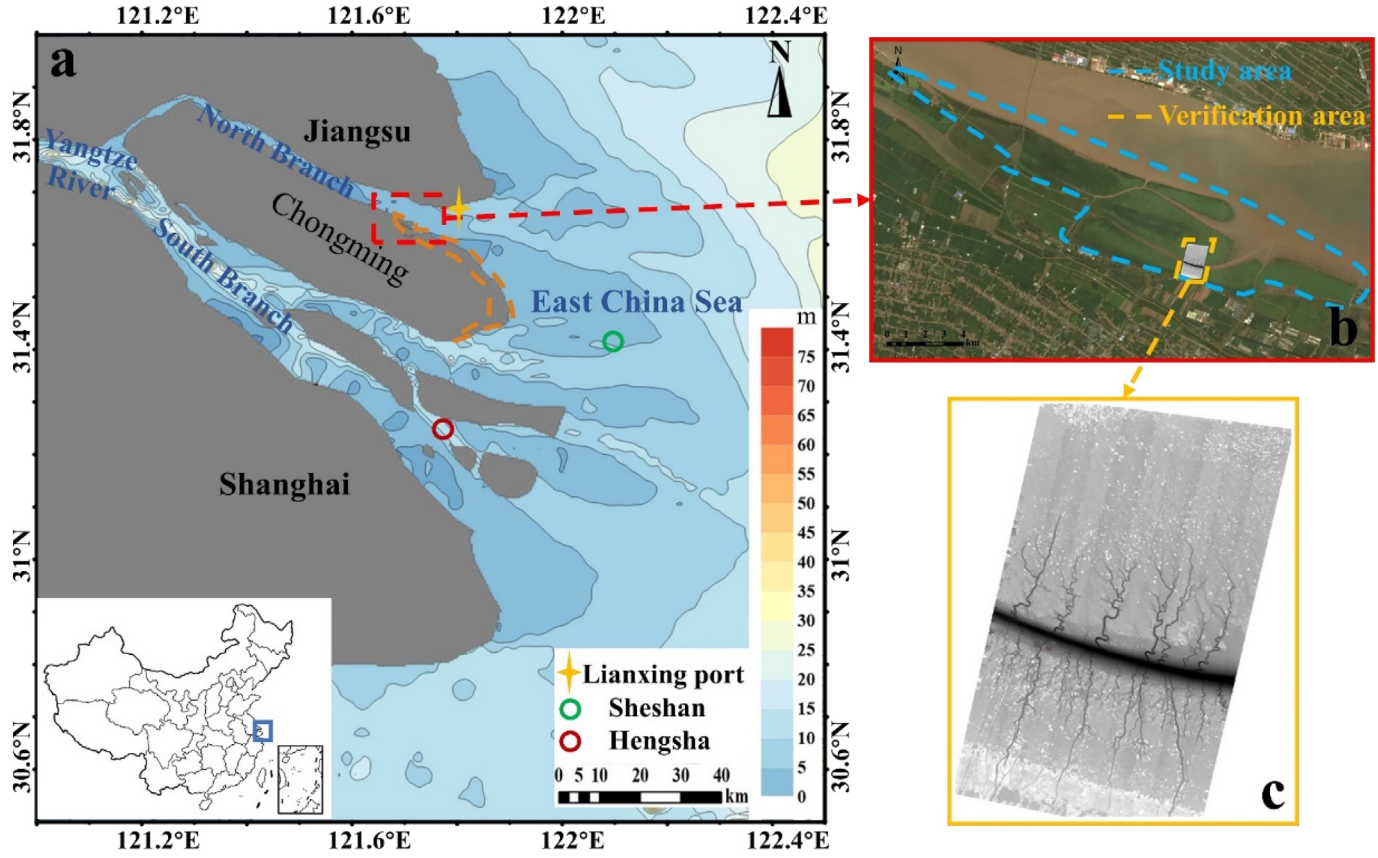

Fig. 1. (a) Study area location. The green and red circles denote the Sheshan and Hengsha tide-gauge station locations, respectively, the yellow star denotes Lianxing port tide-gauge station, and the orange dashed line denotes Chongming-Dongtan. The water depth legend is also included. (b) An enlarged view of red dash-line square in (a), the study area circled by blue dash-line polygon. (c) An enlarged view of the UAV-based LiDAR scanning area selected as the verification area indicated by the yellow dashed line in (b).

2.4. LiDAR scanning data

On the same day (17 August 2019), the GF-1/WFV remote sensing images were acquired and a hexarotor UAV-borne LiDAR system was utilised to obtain the point cloud data of the verification area (Fig. 1c, approximately 2 km^2). The LiDAR system adopts "hummingbird" Genius LiDAR manufactured by SureStar (Beijing, China) and the "ZR-M66" hexarotor-UAV manufactured by ZhiRuiZhiKong Co., Ltd. (Xiamen, China). The "hummingbird" LiDAR utilises a multi-echo technique, which can effectively penetrate the intertidal wetland vegetation and obtain high-precision point cloud data of the intertidal wetland. The system has maximum measuring distance and sailing height of 250 and 150 m, respectively. The experiment was divided into 10 flight strips with a total route length of approximately 23 km, and the obtained .LAS format data included a total of 287.31 million-point clouds. The overall horizontal and vertical accuracies of the point clouds were approximately 0.02 and 0.05 m, respectively.

Table 1
Tidal level data measured at the Lianxing port tide-gauge station and the corresponding remote sensing image data.

Satellite	Image date	Time	Tidal level (m)	Satellite	Image date	Time	Tidal level (m)
GF-1/WFV	24/1/2019	11:10	2.47	GOCI	17/8/2019	08:30	0.98
	11/5/2019	11:17	1.15		17/8/2019	09:30	2.11
	4/6/2019	11:02	3.79		17/8/2019	10:30	3.22
	12/8/2019	10:44	3.08		17/8/2019	11:30	3.93
	17/8/2019	11:05	3.71		17/8/2019	12:30	4.19
	11/11/2019	11:00	4.34				
	13/12/2019	10:40	3.94				

3. Methodology

3.1. Satellite image preprocessing

The GF-1/WFV and GOCI images were preprocessed separately. The GF-1/WFV images were reprojected, and then the coordinate system and projection were set to GCS WGS 1984 and UTM zone 51 N, respectively. The GOCI images were preprocessed utilising the GDPS software. The geographic lookup table file was generated using the resources available at http://kosc.kiost.ac.kr/eng/ by utilising the longitude and latitude information data file of the GOCI images and the generated file was then utilised for geometric correction.

3.2. Spatial-temporal data fusion

To obtain a high-quality intertidal wetland terrain elevation, the WDM requires high spatial resolution satellite images to ensure the accuracy of the DTM. For waterline extraction, however, the revisit period of satellite image is required to be short enough to capture the dynamics of rapid changing intertidal wetland elevation (Niedermeier et al., 2005). Therefore, in this study, the STARFM algorithm proposed by Gao et al. (2006) was used to fuse the high spatial resolution GF-1/WFV data with the high temporal resolution GOCI data to improve the spatial-temporal resolution of the imagery.

The STARFM algorithm is one of the most widely utilised spatial-temporal data fusion models, which considers spatial and time differences in the data fusion process. The STARFM utilises a moving window and a weight function to predict the central pixel value of the window by introducing information on adjacent and similar pixels in the window. The algorithm considers the GF-1/WFV and GOCI image errors invariant when observing the same ground target. The errors depend on

the characteristics of a single pixel and are systematic within a short time interval; therefore, if a pair of GF-1/WFV – GOCI images, obtained at a certain time, serves as a benchmark, the error of each pixel in the image can be estimated. Then, the GOCI images obtained at other times can be utilised to predict their fine-resolution images.

In this study, 1 GF-1/WFV image (acquired at 11:05) and 8 GOCI image scenes (acquired at 8:30, 9:30, 10:30, 11:30, 12:30, 13:30, 14:30, and 15:30) were band-matched and fused utilising the STARFM, and 8 fusion images with a spatial resolution of 16 m were generated. As illustrated in Fig. 2, the STARFM algorithm first resamples the GOCI images after geometric correction and registration to the GF-1/WFV image with a resolution of 16 m. Then, the STARFM generates the fused images.

3.3. TPXO8 tidal model and its applicability

The TPXO tide model is an inversion assimilation model created by Oregon State University, USA. TPXO8 is a modified version of the TPXO model and an inversion assimilation model of altimeter data. TPXO8 further makes harmonic analysis on TOPEX/Poseidon and JASON-1/2 altimeter data and provides the tidal harmonic constants of eight main tidal components (M2, S2, N2, K2, K1, O1, P1, and Q1), with a resolution of $1/30^{\circ} \times 1/30^{\circ}$ (Egbert et al., 1994; Egbert and Erofeeva, 2002).

The TPXO8 model, which can calculate tidal levels in coastal oceans located in areas with an insufficient number of tide-gauge stations, is suitable for areas with complex topography and shallow water and has higher prediction accuracy in the coastal areas of China (Zhao et al., 2018; Fan, 2019). The MATLAB toolbox code for the TPXO8 model can be obtained from the Oregon State University TPXO Tide Model (https://www.tpxo.net/home). Accurate position coordinates and time information were input into the TPXO8 model to obtain the tidal level data.

There are several tide-gauge stations in the Yangtze Estuary that have been engaged in long-term acquisition of continuous, sufficient tidal level data; two such stations (Sheshan and Hengsha) were located close to the study area (Fig. 1a) and were thus selected to evaluate the accuracy of the TPXO8 model.

Owing to the sampling date of 17 August 2019, the TPXO8 model was evaluated utilising the tidal level data of the two tide-gauge stations from 16 to 30 August 2019 (during spring tide), indicating a 15 days period (i.e. one tidal cycle). Hourly tidal data from the Sheshan and Hengsha stations were extracted over this period, and 720 data points were obtained.

The tidal level data derived by using the TPXO8 tidal model were compared with the tide table data (published by the China Maritime Safety Administration and it was assumed to be accurate and error-free) for the corresponding times, as shown in Fig. 3. The mean absolute errors of the TPXO8 model for the two stations were 0.13 and 0.30 m, respectively, and the average error was 0.215 m, which is an acceptable value. Zhao et al. (2018) and Fan (2019) also verified the accuracy of their study and deemed the results reliable.

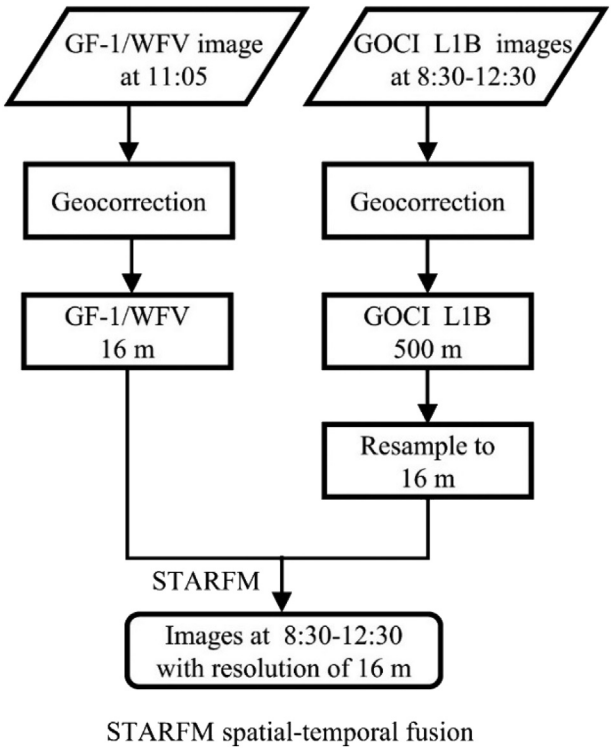

Fig. 2. STARFM spatial-temporal fusion flowchart.

3.4. BP neural network for waterline extraction

As the data sources utilised in this study were passive, non-stereo, optical remote sensing images, the WDM method was used to construct the DTM. To extract the waterline automatically, the supervised classification method in ENVI5.5 (trial version) based on the BP neural network was utilised. The BP neural network is composed of an input and an output layer, and a hidden layer present between the two former layers.

The input, hidden, and output layers correspond to the selected intertidal wetland and water supervision samples, the neural network supervision classification process, and the supervision classification (intertidal wetland and water body) result, respectively. The hidden layer was used to learn the characteristics of the input layer and then used to perform the classification. For example, pixel values of 0 and 1 were established for intertidal wetlands and water bodies, respectively, and classification was performed in a pixel-by-pixel manner. As shown in Fig. 4, two regions of interest, intertidal wetland and water body, were first selected as training samples in the waterline extraction process. Then, the images were classified by using the BP neural network utilising ENVI5.5 (trial version) based on the characteristics of the training samples (i.e. supervised classification). Through iterations, the error was gradually reduced, and the separability of the final sample exceeded 1.9. Generally, if the difference between the two classes is remarkable, the maximum separability of the sample is 2.0. In the study area, the difference between the intertidal wetland and the water body was not evident; therefore, if the separability of the sample was greater than 1.9, the distinction was considered acceptable (He and Zhou, 2018). The intertidal wetland and water body were classified, and the boundary between them was considered the waterline.

The waterline is regarded as the elevation line of the intertidal wetland, which changes with tidal flooding and ebbing. Therefore, a series of waterline contours extracted from time-series satellite images with various elevation values (tidal levels) form a series of seashore terrain isoclines and can be interpolated to construct a DTM. The tidal level data utilised in this study was generated using the TPXO8 tidal model and the measurements obtained at the Lianxing port tide-gauge station.

3.5. DTM construction using waterline and LiDAR point cloud data

3.5.1. DTM construction using waterline data

The DTM was constructed using waterline contours utilising the triangulated irregular network (TIN) option in ArcGIS10.1 (Fig. 5), which uses Delaunay triangulation to connect irregularly spaced elevation point data. The elevation triangles were then interpolated to a grid-based DTM. As the TIN method generates triangles according to the sample point locations, and because more sample points are likely located in deep slopes than flat areas, the TIN model can accurately reflect the terrain by avoiding redundancies in flat areas.

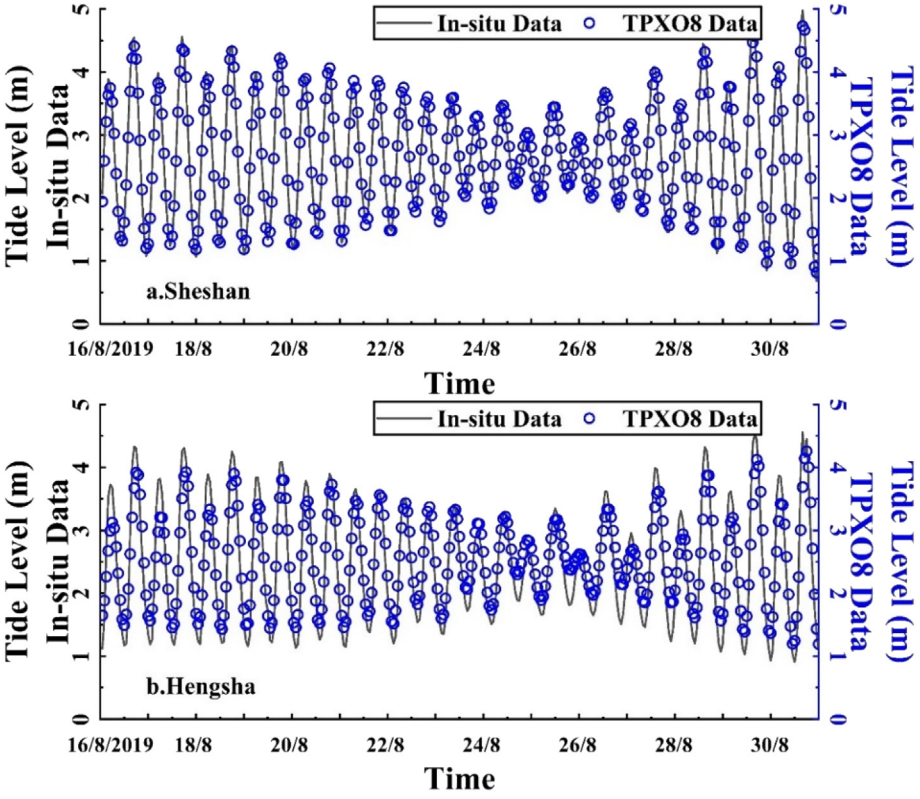

Fig. 3. Verification of the TPXO8 model utilising tidal level data from the (a) Sheshan and (b) Hengsha stations. The solid black line represents the in-situ data, and the blue circles represent the TPXO8 data.

The specific operation was realized in ArcGIS10.1 as follows. First, each waterline was assigned a tidal level value, and then a TIN was created by selecting "Create TIN" in the 3D analyst extension module of ArcGIS10.1. Next, "TIN to Raster" was selected in the 3D analyst extension module of ArcGIS10.1 to convert the TIN into a grid to obtain the corresponding DTM data.

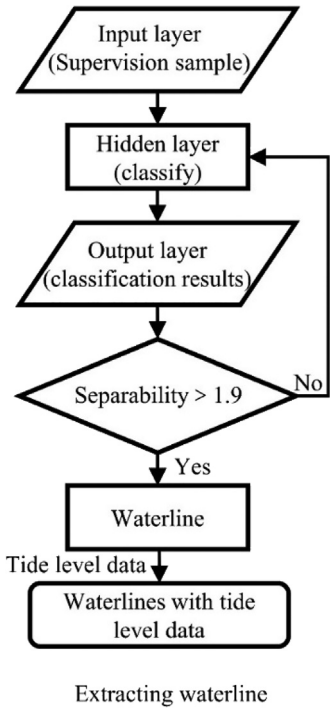

Fig. 4. Waterline extraction process flowchart.

3.5.2. DTM construction using LiDAR point cloud data

The LiDAR terrain elevation data were generated utilising the original UAV-borne LiDAR data (Fig. 5). First, using the cloth simulation filtering algorithm in CloudCompare, the original .LAS data were filtered to remove the vegetation and noise points, and the ground points were saved in an .XYZ format. Then, the .XYZ data (ground points) were imported into LiDAR360 (trial version) to generate the preliminary DTM. Next, the preliminary DTM was converted to a TIN by selecting "Create TIN" in LiDAR360 (trial version), which was then converted to a .TIF file with both XSize and YSize set to 2 and buffer size set to 5. As noise points such as those attributed to vegetation remained in the data, median filtering was performed using ENVI5.5 (trial version). The "Convolutions and Morphologies" of "Filter" file was selected and the median filtering was conducted with the kernel size set at 3, which effectively reduced noise in the image. Finally, the DTM constructed using the LiDAR point cloud data was utilised as the ground truth to evaluate the vertical accuracy of the proposed method.

3.6. Summary of all procedures

The proposed method utilised in this study includes four processes (Fig. 6). First, the GF-1/WFV and GOCI data were fused utilising the STARFM (Gao et al., 2006) to obtain multispectral images with 16 m spatial resolution and 1 h temporal resolution, from which, terrain elevation data with a 1 days period were obtained via interpolation. Second, tidal level data were obtained from the tidal model or tide-gauge stations. Third, the intertidal wetlands and water bodies in the satellite images were classified utilising the supervised classification method of the BP neural network, and then the waterline was extracted. Fourth, tidal level data were

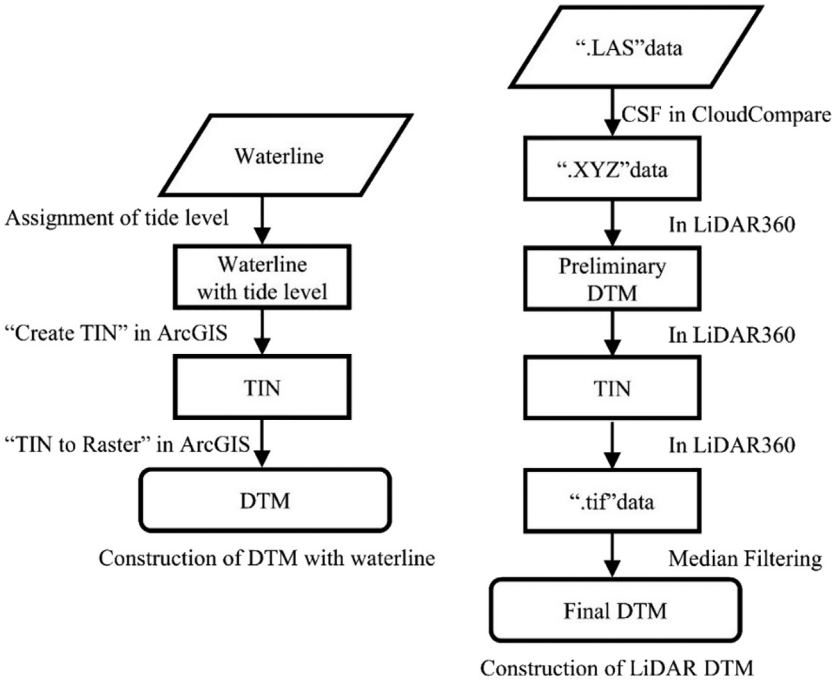

Fig. 5. Flowchart of DTM construction using waterline data.

correspondingly assigned to a series of waterline contours, and then the DTM was constructed utilising the TIN method.

4. Results

4.1. Satellite waterline extraction and DTM construction

The WDM for the 6 images was on 17 August 2019, which included 1 GF-1/WFV (acquired at 11:05) and 5 multi-source satellite fusion (acquired at 8:30, 9:03, 10:30, 11:30, and 12:30) images, they were performed to extract a series of waterline contours, as shown in Fig. 7. In the 8:30–12:30 period, the tidal level gradually increased, and the waterline contours gradually approached from the sea to the land.

The DTM (Fig. 8) was constructed utilising waterline contours from hourly time-series satellite images and the measured tidal level data obtained from the Lianxing port tide-gauge station (hereafter referred to as DTM_{sat}). The DTM_{sat} range was 1.64–4.50 m and the theoretical depth datum was utilised as the datum plane. The elevation decreased from the southwest (land) to the northeast (sea) direction.

4.2. LiDAR DTM construction

The DTM was constructed utilising LiDAR point cloud data acquired by using a UAV-borne LiDAR system (hereafter referred to as DTM_{LiD}). As shown in Fig. 9a, certain vegetation points could not be removed by using the cloth simulation filtering algorithm, which presented as noise points in the DTM_{LiD}. These noise points were removed by conducting median filtering, which improved the DTM_{LiD} image quality (Fig. 9b).

4.3. DTM validation

The DTM_{LiD} was considered the ground truth and utilised to validate the synchronous satellite constructed DTM. The DTM_{LiD} was constructed using LiDAR data obtained on 17 August 2019, and the satellite DTM was based on a series of waterlines extracted from hourly time-series satellite fusion images acquired on 17 August 2019. The satellite DTM was constructed utilising the waterline contours determined by the tidal level data obtained from the Lianxing port tide-gauge station (DTM^{s}_{sat}) and the TPXO8 generated tidal level data (DTM^{m}_{sat}) to evaluate the accuracy of both satellite DTMs. Particularly, this study attempted to assess the DTM^{m}_{sat}, even without measured tidal level data.

As shown in Fig. 10a and b, the spatial distributions of the differences between DTM_{LiD} and DTM^{s}_{sat} (DTM_{LiD} - DTM^{s}_{sat}) and between DTM_{LiD} and DTM^{m}_{sat} (DTM_{LiD} - DTM^{m}_{sat}) are similar, with an error range of −0.80 to 0.60 m, and the peak value of DTM_{LiD} - DTM^{m}_{sat} is slightly lower than that of DTM_{LiD} - DTM^{s}_{sat}. The positive difference between the southernmost zone, shown in orange in Fig. 10a and b, is relatively large and corresponds to the southernmost highlight zone shown in Fig. 1c. The most considerable difference is attributed to the influence of dense vegetation in this zone on the LiDAR data. The green areas (occupying the most area) in Fig. 10a and b, showing a positive error of 0.2 m more or less, mainly occur in flat areas.

Negative errors mainly occur in tidal trenches, which are represented as blue-coloured and violet-coloured areas in Fig. 10a and b, and the deeper the trench, the greater the negative error. For example, a large tidal trench is evident in the middle of Fig. 10a and b (the violet-coloured area) where the error reaches −0.7 m. This is because the spatial resolution of the satellite data is still lower than that of the

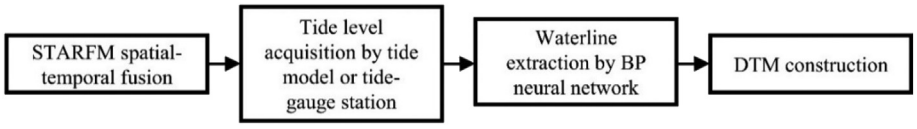

Fig. 6. Proposed methodology.

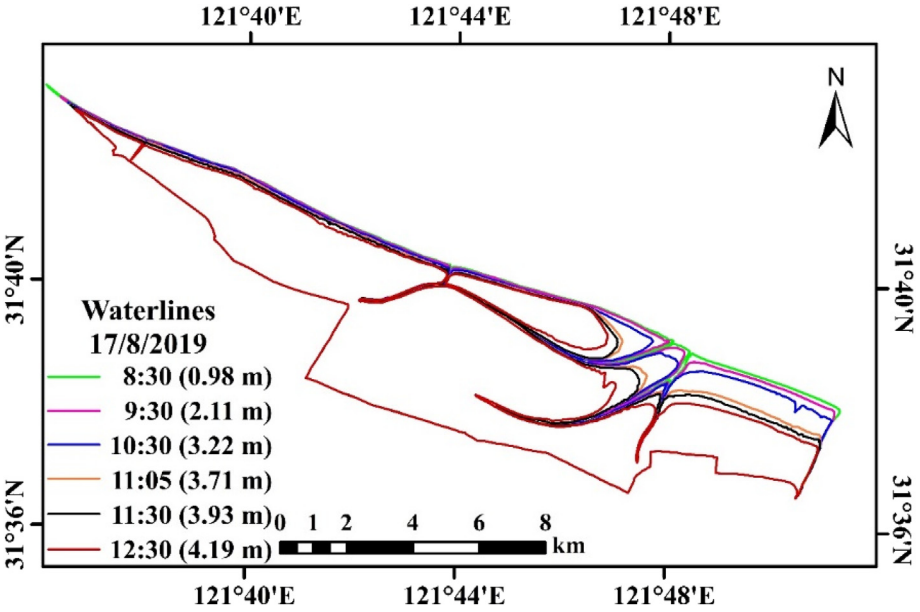

Fig. 7. Waterline contours, generated using 6 time-series satellite images, observed in the North Branch intertidal wetland of Chongming Island. The 6 waterline contours were extracted from images acquired at 8:30, 9:30, 10:30, 11:05, 11:30 and 12:30, corresponding to tidal levels of 0.98, 2.11, 3.22, 3.71, 3.93 and 4.19 m.

LiDAR data, which poses challenges in meeting the DTM construction requirements for tidal trenches. Additionally, the terrain only changes vertically, not horizontally (such as ditches or cliffs), which is challenging for DTM construction and causes substantial errors in the modelling of tidal trenches.

Statistical analyses of the DTM^{s}_{sat} and DTM^{m}_{sat} errors were performed in a pixel-by-pixel manner, and the results, shown in Fig. 10c and d, represent a normal distribution. Fig. 10c shows that 27% and 86% of the pixels were distributed in the range of −0.10 to 0.10 and − 0.30 to 0.30 m, respectively, with a root mean square error (RMSE) of 0.22 m. Fig. 10d shows that 65% and 93.63% of the pixels were distributed in the range of −0.10 to 0.10 and − 0.30 to 0.30 m, respectively, with an RMSE of 0.16 m. The RMSE of the DTM^{m}_{sat} is slightly lower than that of the DTM^{s}_{sat}, which implies that the accuracy of the satellite DTM constructed utilising the tidal levels simulated by the TPXO8 model is acceptable. Therefore, utilisation of the TPXO8 modelled tidal level data for satellite DTM construction is suitable for areas without tide-gauge stations.

4.4. Annual dynamic change of the DTM

To explore the influence of the time scale on the DTM, the proposed method in this study was used to investigate the annual variation of the DTM in the intertidal wetland located in the eastern region of Chongming Island spanning from 121°47′E–122°05′E to 31°25′N–31°38′N (Chongming-Dongtan, the area denoted in the dashed orange line in Fig. 1a), which is the most widely developed tidal flat in the Yangtze Estuary and one of the most important wetlands in the world.

An hourly time-series analysis of 6 fusion images obtained on 18 December 2018 (acquired at 8:30, 9:30, 10:30, 11:09, 11:30, and 14:30) and another hourly time-series analysis of 6 fusion images obtained on 13 December 2019 (acquired at 8:30, 9:30, 10:30, 10:40, 11:30,

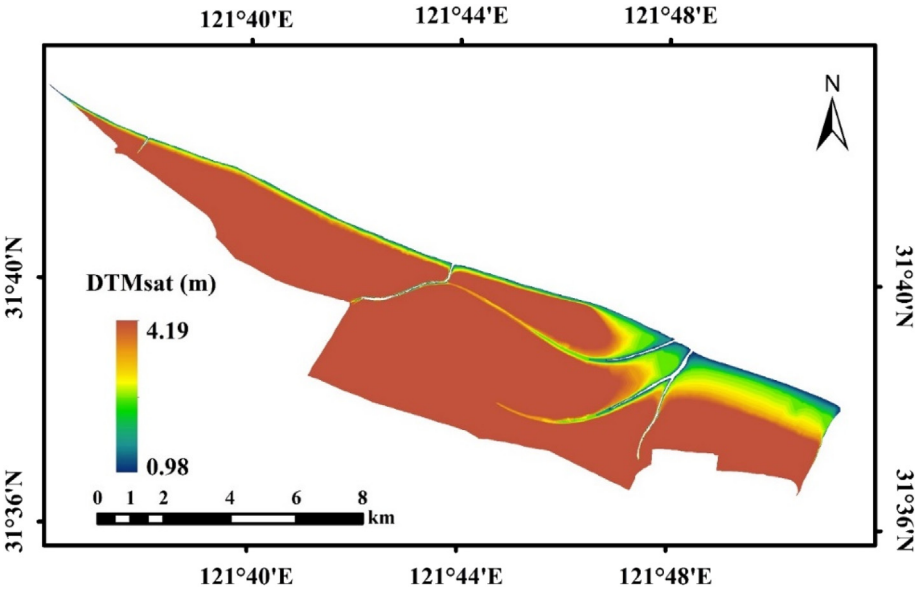

Fig. 8. DTM of the North Branch intertidal wetland of Chongming Island. Tidal level data was obtained from the Lianxing port tide-gauge station.

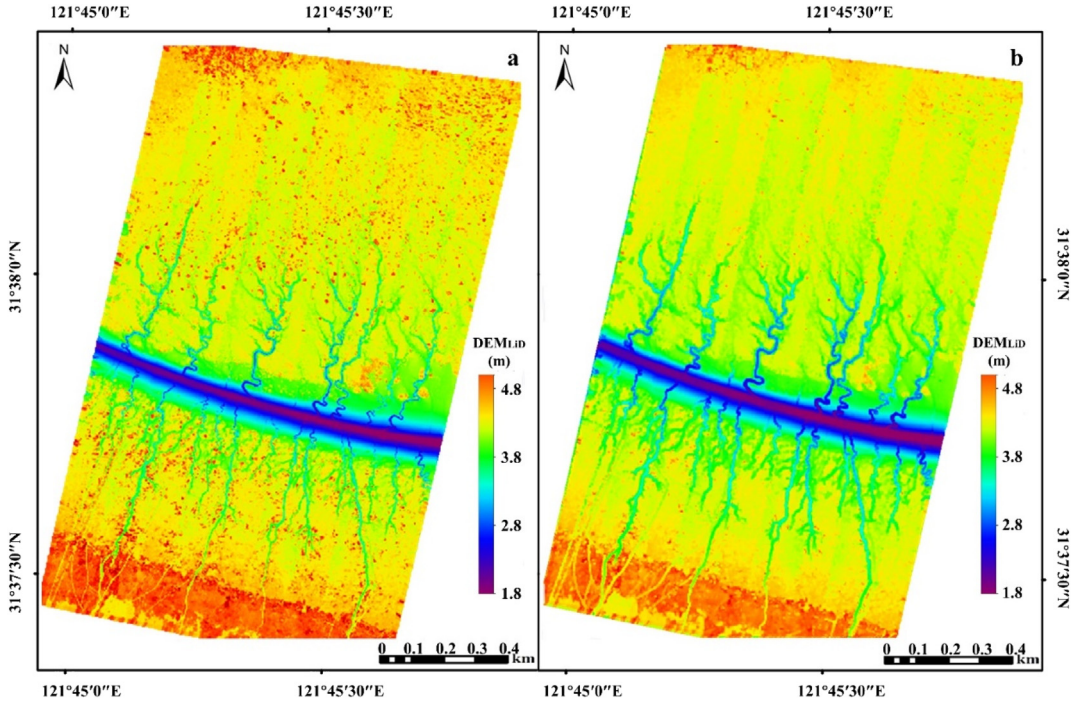

Fig. 9. LiDAR DTM (a) before and (b) after median filtering.

13:30) were generated by using the spatial-temporal fusion method. Two groups of waterline contours were extracted using each of the hourly time-series images and utilised to construct the daily DTMs for 2018 and 2019 (Fig. 11a and b, respectively). Here, the waterline contour elevation values were determined by the TPXO8-modelled tidal levels because no tide-gauge station was present in the vicinity.

The 2019 DTM elevations were significantly higher than the 2018 DTM elevations. Fig. 11c shows the differences between the two DTMs, which generally exceed zero, and are greater than 0.7 m in the northern part (area inside the red-dashed rectangle in Fig. 11c). This implies that siltation rate in the northern part was faster than the rest of study area. The results of the statistical analysis performed in a pixel-by-pixel manner (Fig. 11d) indicate that the difference values less than and greater than 0 m accounted for 18.4% and 81.6%, respectively. Among them, 47.8% and 16.2% range from 0 to 0.2 and 0.2–0.4 m, respectively, and 17.6% are greater than 0.4 m, indicating that some regions undergo significant changes (e.g. in the northern part in Fig. 11c). The DTM of Chongming-Dongtan changed significantly within one year from 2018 to 2019.

It is assumed that the DTM constructed using waterline contours extracted from time-series images does not change within the period of acquisition of the time-series images. It implies that the period of time series images should be as short as possible in order to ensure the stability of DTM. Therefore, the proposed high-resolution spatial-temporal fusion approach is a novel method that yields hourly time-series images and generates a daily DTM in the shortest period.

5. Discussion

5.1. Spatial resolution influences DTM accuracy

Zhang et al. (2016) determined that the spatial resolution of an image plays an important role in the resolution of the DTM, and the higher the DTM resolution, the more accurately it represents the terrain features. A pixel may contain more than one type of ground object in a relatively low spatial resolution image, which affects the accuracy of the waterline extracted from the image.

To quantify the influence of spatial resolution on DTM accuracy, high- and low-resolution images (GF-1/WFV image with 16 m and GOCI image with 500 m, respectively) were selected for the waterline extraction. As shown in Fig. 12b, the waterline (red line) extraction from the GOCI image can be influenced by the presence of mixed pixels due to low resolution, thus potentially causing a considerable bias in the waterline location. In comparison, waterline (indicated by red line in Fig. 12c) extraction from the GF-1/WFV image is less influenced by the presence of mixed pixels, thereby providing a more accurate location. The maximum horizontal distance between the two waterlines was 372.9 m. The average distance between the two lines was 134.6 m, which was calculated by dividing the area between the two lines by the straight-line distance between the two ends of the line utilising ArcGIS10.1. The slope of the studied intertidal wetland was 0.15°, and an error of 134.6 m in the horizontal distance might produce an error of 0.35 m in the vertical elevation; therefore, the spatial resolution of the satellite images has a significant impact on the accuracy of the DTM.

The higher the spatial resolution of the satellite image, the higher the accuracy and reliability of the DTM construction. Satellite images such as those obtained by using Landsat-8/OLI, Sentinel-2/MSI, and GF-1/WFV are considered high spatial resolution data sources. A GF-1/WFV image, with a 16 m spatial resolution and a 4 days revisit frequency, is superior to Landsat series images, and its 800 km width is superior to that of a Sentinel-2/MSI image, which is particularly important for intertidal wetlands located in large estuaries and on coasts, thereby making it an ideal high-resolution data source.

5.2. Time scale influences on the DTM

A DTM is constructed utilising a series of waterline contours extracted from time-series images; however, due to the influence of low revisit frequency and cloud cover, the number of satellite images with high spatial resolution is markedly limited. It is difficult to acquire time-series images and extract a series of water contours from high to low tide in a short period. Liu et al. (2012) extracted a series of waterline contours using multi-source satellite images acquired over a period of one year, and Khan et al. (2019) obtained a series of waterline contours

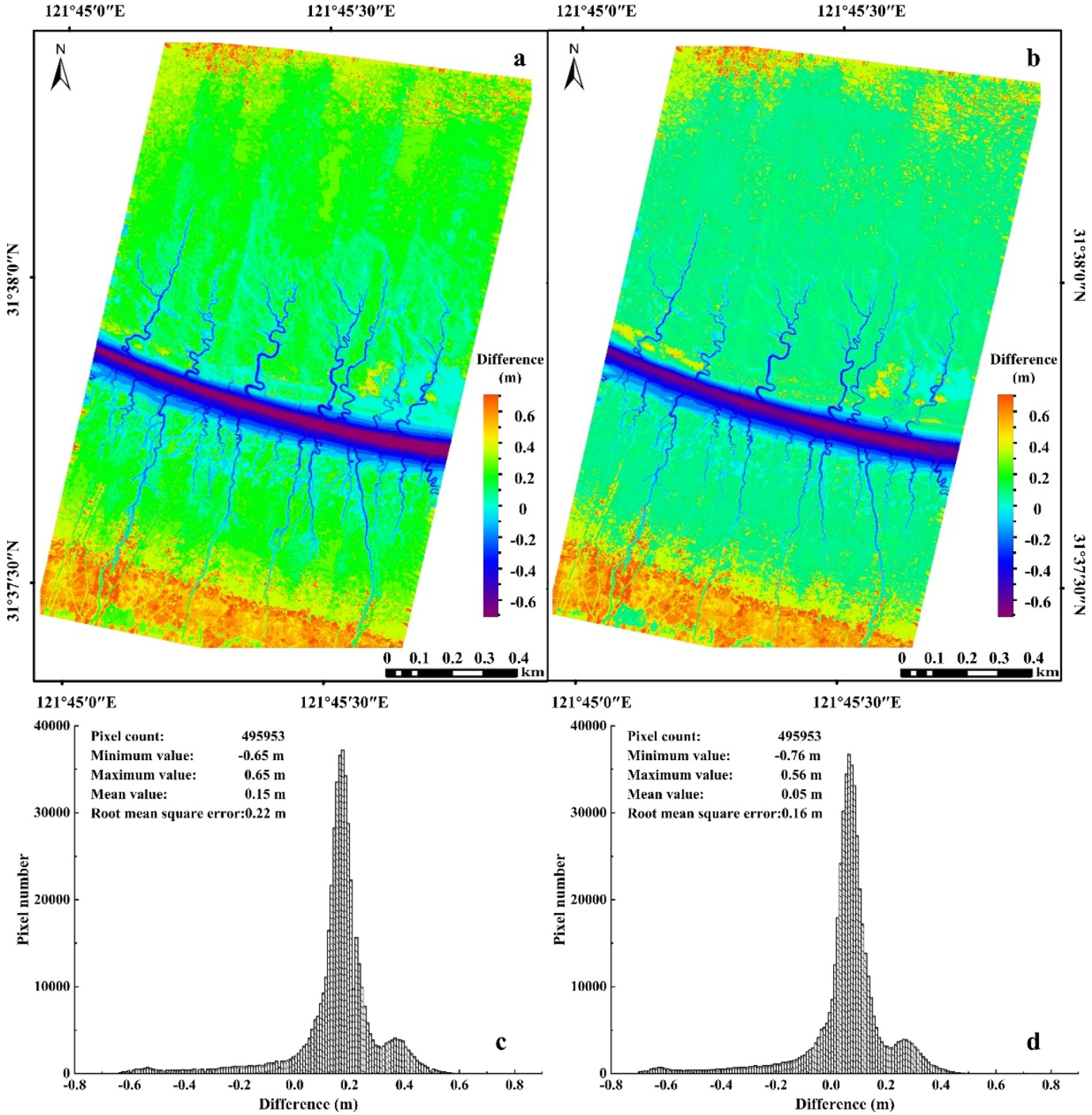

Fig. 10. (a) Difference between DTM_{LiD} and DTM^{s}_{sat} (DTM_{LiD} - DTM^{s}_{sat}) and (b) difference between DTM_{LiD} and DTM^{m}_{sat} (DTM_{LiD} - DTM^{m}_{sat}). DTM^{s}_{sat} and DTM^{m}_{sat} were obtained using the tidal level data measured at the Lianxing port tide-gauge station and the TPXO8-modelled tidal level data, respectively. (c and d) The two statistical deviations corresponding to the differences in (a) and (b), respectively.

and constructed a DTM using Sentinel-2/MSI images acquired over a period spanning three years.

To explore the time scale influence of time-series image acquisition on the DTM, time-series images from two time scales were analysed in this study. One series include 6 GF-1/WFV time-series images acquired over a period of one year from 24 January to 13 December 2019 for waterline extraction to construct the DTM ($DTM_{non\text{-}fusion}$), with the waterline contours determined using tidal level data obtained from the Lianxing port tide-gauge station. The second series include 6 fusion time-series images acquired in one day to construct the DTM (DTM_{fusion}). In this series, the waterline contours were determined using tidal level data obtained from the Lianxing port tide-gauge station on 17 August 2019, so actually DTM_{fusion} is equal to DTM^{s}_{sat} (discussed in Section 4.3), and the synchronous DTM_{LiD} indicates the ground truth. The difference between DTM_{LiD} and $DTM_{non\text{-}fusion}$ (DTM_{LID} - $DTM_{non\text{-}fusion}$) and the statistical analysis for the pixel-by-pixel differences are shown in Fig. 13. In Fig. 13b, 12% and 76% of the pixels are distributed within the range of −0.10 to 0.10 and − 0.30 to 0.30 m, respectively, with an RMSE of 0.27 m. Comparing the absolute errors in Figs. 10c and 13b, the absolute errors of 24% and 14% of the pixels in the $DTM_{non\text{-}fusion}$ and DTM_{fusion}, respectively, exceed

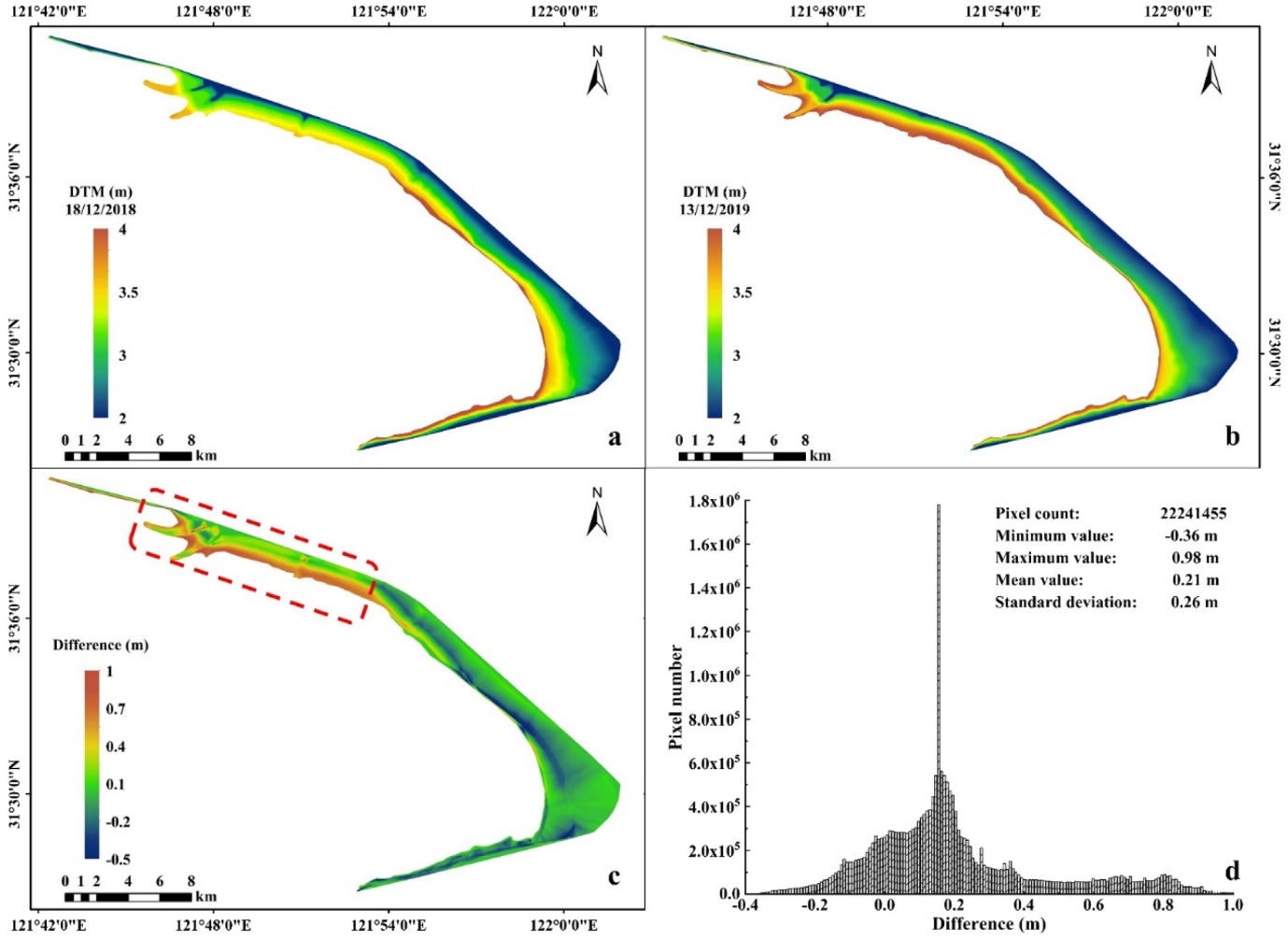

Fig. 11. DTM of Chongming-Dongtan on (a) 18 December 2018 and (b) 13 December 2019. Tidal level information obtained by using the TPXO8 tidal model. (c) Differences between the 2018 and 2019 DTM values and (d) differences presented with pixel statistics.

0.3 m. This implies that the $DTM_{non\text{-}fusion}$ error includes annual variation of terrain elevation.

Sediment discharge in the Yangtze Estuary varies with the flood and dry seasons and is influenced by human activity (Shen et al., 2013). The intertidal wetland terrain elevations in the Yangtze Estuary change rapidly, regionally, and unsteadily. As discussed in Section 4.4, there are annual variations observed in the terrain elevations of Chongming-Dongtan. Fig. 12c shows that terrain elevation of Chongming-Dongtan changed remarkably from December 2018 to December 2019, and the average and maximum elevation variations during this period were 0.21 and 0.98 m, respectively. Therefore, utilising time-series images on a long-term scale (e.g. one year) to construct the DTM is not appropriate, especially for rapidly changing intertidal wetlands.

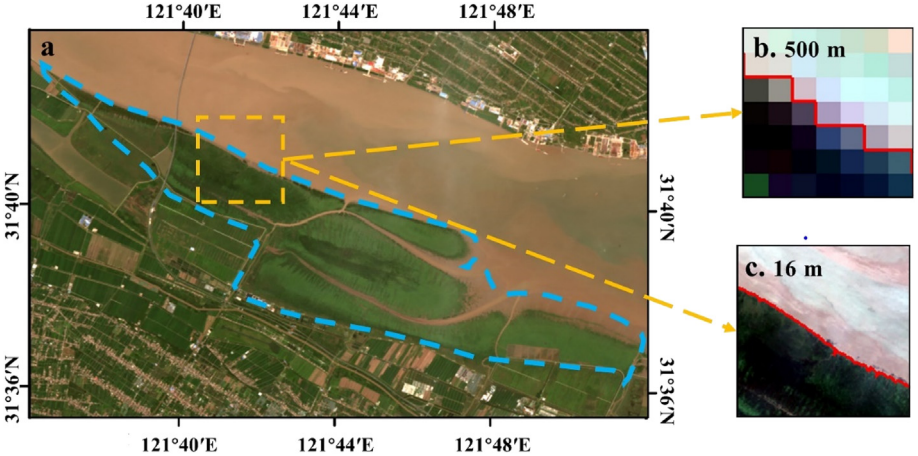

Fig. 12. (a) Location of the waterline extracted using a satellite image with (b) low-resolution (500 m) and (c) high-resolution (16 m).

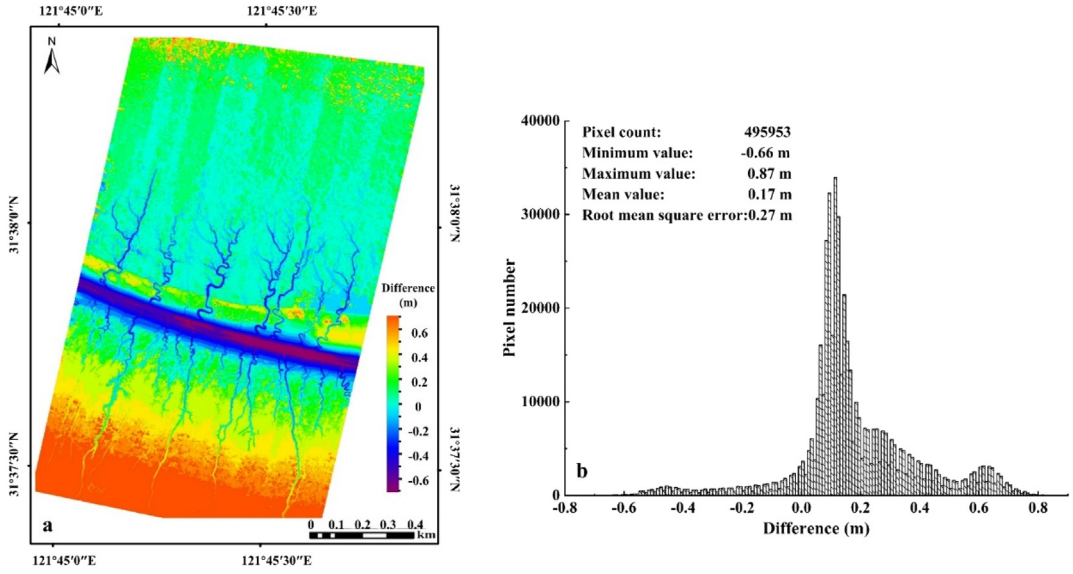

Fig. 13. (a) Difference between the yearly DTM_{LID} and $DTM_{non\text{-}fusion}$ (DTM_{LID} - $DTM_{non\text{-}fusion}$) and (b) statistical deviations corresponding to the differences.

5.3. Limitations

A limitation exists for the spatial-temporal fusion model. The STARFM proposed by Gao et al. (2006) depends on the characteristic patch size of the pixel, which would be degraded by extremely heterogeneous fine-grained pixels. This limitation also existed in this study, the STARFM could capture detail changes in most regions, but some regions with large spatial heterogeneity and intense horizontal motion might not be accurately predicted. Pan et al. (2018) indicated that the STARFM algorithm could not detect changes when two contradictory changes occurred simultaneously in coarse-resolution pixels and compensated each other. Additionally, the STARFM algorithm ignores the geographical location error that always exists. For example, the registration of two images observed by different sensors will produce geographic location errors.

In the study area, the tidal trench width is generally less than 10 m; therefore, the spatial resolution of images less than 10 m cannot meet the tidal trench terrain detection accuracy requirements. As illustrated in Fig. 10, the DTM error of the tidal trench terrain increased with decreasing distance from the tidal channel. The DTM_{sat} error of the tidal trench terrain is greater than the DTM_{LiD} error, which is due to the low spatial resolution of the satellite image.

The waterline contours utilised in the DTM construction were determined by using the tidal level data and were affected by the highest and lowest tidal levels. The DTM constructed in the area between the highest and lowest tidal levels was more accurate; however, while the DTM constructed outside the mentioned area was rougher. For example, the dark red area in Fig. 8 takes quite a big part, and is located beyond the waterline with the highest tidal level and is not flooded by water. The reason is related to the highest tidal level assigned to the waterline contour for the DTM construction using satellite images. For example, at 12:30 on 17 August 2019, the highest tide level measured at Lianxing port station was 4.19 m and the maximum elevation of the satellite DTM was 4.19 m. If the LiDAR detects a terrain elevation change in this area, the DTM constructed from satellite and LiDAR data in this area will have a considerable deviation.

6. Conclusion

In this study, the spatial-temporal fusion of high spatial resolution GF-1/WFV data and high temporal resolution GOCI data was performed to generate hourly time-series images with a spatial resolution of 16 m at different high- and low-tide phases. This method solved the problem of limited number of high spatial resolution satellite image time series due to influences of cloud cover and low revisit frequency. And this method ensures that the images have high temporal and spatial resolution at the same time.

The DEM is constructed utilising a series of waterline contours extracted from satellite image time series. The neural network supervised classification method with high accuracy is proposed for the waterline extraction. The accuracy of waterline extraction is also affected by the spatial resolution of satellite imagery. The position difference of the waterline obtained by using the 16- and 500-m resolution images was approximately 134.6 m in the study area, so that there may be an error of 0.35 m in DTM based on the tidal flat slope of 0.15°. Generally, higher spatial resolution satellite images will produce more accurate results of waterline extraction.

By comparing the two DTMs, one is the DTM_{fusion} constructed by using hourly time-series fusion images (i.e. daily DTM), the other is the $DTM_{non\text{-}fusion}$ constructed by using time-series GF/WVF images within one year (i.e. yearly DTM). It is found that the $DTM_{non\text{-}fusion}$ error (with an RMSE of 0.27 m) observed is greater than the DTM_{fusion} error (with an RMSE of 0.22 m), which implies that the $DTM_{non\text{-}fusion}$ error includes the offset caused by the terrain elevation change. The daily DTM is synchronously validated by using the terrain elevation data acquired utilising a UAV-borne LiDAR in the study area, with RMSEs of 0.16 and 0.22 m for the modelled and measured tidal level data, respectively.

Through the application of high spatial-temporal resolution satellite image fusion method we proposed in the Chongming-Dongtan, it is found that a significant change in the DTM occurred from 2018 to 2019 and the DTM increase in the northern part of Chongming-Dongtan exceeded 0.7 m. This proved that the time scale of the time-series images influences on DTM. This method effectively reduces the influence of time-series and spatial resolution on DTM, and is effective for monitoring high dynamic changes in intertidal wetland terrain elevations.

Declaration of competing interest

The authors declare that they have no known competing financial interests or personal relationships that could have appeared to influence the work reported in this paper.

Acknowledgement

This work was supported by the Science and Technology Commission of Shanghai Municipality (Grant No. 18DZ1206401), the National Key Research & Development Program of China (Grant No. 2017YFE0107400), and the National Natural Science Foundation of China (Grant No. 41771378). We are grateful to Dr. Yanqun Pan for his assistance with the spatial-temporal data fusion, and the two anonymous reviewers and the editor for their constructive comments and suggestions. We thank Beijing Green Valley Technology Co., Ltd. and the United States ITT VIS Co. for providing the trial versions of LiDAR360 and ENVI5.5, respectively.

References

Almeida, L.P., Almar, R., Bergsma, E.W.J., Berthier, E., Baptista, P., Garel, E., Dada, O.A., Alves, B., 2019. Deriving high spatial-resolution coastal topography from sub-meter satellite stereo imagery. Remote Sens. 11, 590. https://doi.org/10.3390/rs11050590.

Anthony, E.J., Dolique, F., Gardel, A., Gratiot, N., Proisy, C., Polidori, L., 2008. Nearshore intertidal topography and topographic-forcing mechanisms of an Amazon-derived mud bank in French Guiana. Cont. Shelf Res. 28, 813–822. https://doi.org/10.1016/j.csr.2008.01.003.

Bai, Z., 2013. Technical characteristics of Gaofen-1 satellite. Aerosp. China 5–9.

Benveniste, J., Cazenave, A., Vignudelli, S., Fenoglio-Marc, L., Shah, R., Almar, R., Andersen, O., Birol, F., Bonnefond, P., Bouffard, J., Calafat, F., Cardellach, E., Cipollini, P., Le Cozannet, G., Dufau, C., Fernandes, M.J., Frappart, F., Garrison, J., Gommenginger, C., Han, G., Høyer, J.L., Kourafalou, V., Leuliette, E., Li, Z., Loisel, H., Madsen, K.S., Marcos, M., Melet, A., Meyssignac, B., Pascual, A., Passaro, M., Ribó, S., Scharroo, R., Song, Y.T., Speich, S., Wilkin, J., Woodworth, P., Wöppelmann, G., 2019. Requirements for a coastal hazards observing system. Front. Mar. Sci. 6. https://doi.org/10.3389/fmars.2019.00348.

Chen, J., Yun, C., Xu, H., Dong, Y., 1979. The Developmental Model of the Chang Jiang River Estuary during last 2000 years. Acta Oceanol. Sin. 1, 103–111.

Chen, J., Shen, H., Yu, C., 1988. Processes of Dynamics and Geomorphology of the Changjiang Estuary.

Choi, C., Kim, D.J., 2018. Optimum baseline of a single-pass in-SAR system to generate the best DEM in tidal flats. IEEE J. Sel. Top. Appl. Earth Obs. Remote Sens. 11, 919–929. https://doi.org/10.1109/JSTARS.2018.2795107.

Egbert, G.D., Erofeeva, S.Y., 2002. Efficient inverse modeling of barotropic ocean tides. J. Atmos. Ocean. Technol. 19, 183–204. https://doi.org/10.1175/1520-0426(2002)019<0183:EIMOBO>2.0.CO;2.

Egbert, G.D., Bennett, A.F., Foreman, M.G.G., 1994. TOPEX/POSEIDON tides estimated using a global inverse model. J. Geophys. Res. 99, 24,821–24,852. doi:https://doi.org/10.1029/94jc01894.

Fan, C., 2019. Latest advances of global ocean tide models and their accuracy comparisons in coastal areas of China. J. Geod. Geodyn. 39, 476–481.

Gao, F., Masek, J., Schwaller, M., Hall, F., 2006. On the blending of the landsat and MODIS surface reflectance: predicting daily landsat surface reflectance. IEEE Trans. Geosci. Remote Sens. 44, 2207–2218. https://doi.org/10.1109/TGRS.2006.872081.

Ghosh, M.K., Kumar, L., Roy, C., 2015. Monitoring the coastline change of Hatiya Island in Bangladesh using remote sensing techniques. ISPRS J. Photogramm. Remote Sens. 101, 137–144. https://doi.org/10.1016/j.isprsjprs.2014.12.009.

He, M., Wu, J., 2008. Jiuduansha intertidal elevation acquisition based on multi-temporal remote sensing images. Resour. Environ. Yangtze Basin 310–316. https://doi.org/10.1017/CBO9781107415324.004.

He, Y., Zhou, J., 2018. Accuracy comparison of several supervised classification methods in ENVI. Technology Innovation and Application. 22–24.

Irish, J.L., White, T.E., 1998. Coastal engineering applications of high-resolution lidar bathymetry. Coast. Eng. 35, 47–71. https://doi.org/10.1016/S0378-3839(98)00022-2.

Kang, Y., Ding, X., Xu, F., Zhang, C., Ge, X., 2017. Topographic mapping on large-scale tidal flats with an iterative approach on the waterline method. Estuar. Coast. Shelf Sci. 190, 11–22. https://doi.org/10.1016/j.ecss.2017.03.024.

Khan, M.J.U., Ansary, M.N., Durand, F., Testut, L., Ishaque, M., Calmant, S., Krien, Y., Saifu, A.K.M., Papa, F., 2019. High-resolution intertidal topography from sentinel-2 multispectral imagery: Synergy between remote sensing and numerical modeling. Remote Sens. 11, 1–20. https://doi.org/10.3390/rs11242888.

Kirwan, M.L., Megonigal, J.P., 2013. Tidal wetland stability in the face of human impacts and sea-level rise. Nature 504, 53–60. https://doi.org/10.1038/nature12856.

Lee, S.K., Ryu, J.H., 2017. High-accuracy tidal flat digital elevation model construction using tanDEM-X science phase data. IEEE J. Sel. Top. Appl. Earth Obs. Remote Sens. 10, 2713–2724. https://doi.org/10.1109/JSTARS.2017.2656629.

Li, X., Liu, J.P., Tian, B., 2016. Evolution of the Jiuduansha wetland and the impact of navigation works in the Yangtze Estuary, China. Geomorphology 253, 328–339. https://doi.org/10.1016/j.geomorph.2015.10.031.

Liu, Y., Li, M., Cheng, L., Li, F., Chen, K., 2012. Topographic mapping of offshore sandbank tidal flats using the waterline detection method: a case study on the Dongsha Sandbank of Jiangsu Radial Tidal Sand Ridges, China. Mar. Geod. 35, 362–378. https://doi.org/10.1080/01490419.2012.699501.

Liu, Y., Li, M., Mao, L., Cheng, L., Li, F., 2013a. Toward a Method of Constructing Tidal Flat Digital Elevation Models with MODIS and Medium-Resolution Satellite Images. J. Coast. Res. 29, 438. https://doi.org/10.2112/jcoastres-d-12-00088.1.

Liu, Y., Li, M., Zhou, M., Yang, K., Mao, L., 2013b. Quantitative analysis of the waterline method for topographical mapping of tidal flats: a case study in the dongsha sandbank, China. Remote Sens. 5, 6138–6158. https://doi.org/10.3390/rs5116138.

Mason, D.C., Davenport, I.J., Robinson, G.J., Flather, R.A., McCartney, B.S., 1995. Construction of an inter-tidal digital elevation model by the 'Water-Line' Method. Geophys. Res. Lett. 22, 3187–3190. https://doi.org/10.1029/95GL03168.

Mason, D.C., Gurney, C., Kennett, M., 2000. Beach topography mapping - a comparison of techniques. J. Coast. Conserv. 6, 113–124. https://doi.org/10.1007/BF02730475.

Mcfeeters, S.K., 1996. The use of the Normalized Difference Water Index (NDWI) in the delineation of open water features. Int. J. Remote Sens. 17 (7), 1425–1432.

Niedermeier, A., Hoja, D., Lehner, S., 2005. Topography and morphodynamics in the German Bight using SAR and optical remote sensing data. Ocean Dyn. 55, 100–109. https://doi.org/10.1007/s10236-005-0114-2.

Pan, Y., Shen, F., Wei, X., 2018. Fusion of Landsat-8/OLI and GOCI data for hourly mapping of suspended particulate matter at high spatial resolution: a case study in the Yangtze (Changjiang) estuary. Remote Sens. 10 (2), 158. https://doi.org/10.3390/rs10020158.

Purkis, S.J., Gardiner, R., Johnston, M.W., Sheppard, C.R.C., 2016. A half-century of coastline change in Diego Garcia - the largest atoll island in the Chagos. Geomorphology 261, 282–298. https://doi.org/10.1016/j.geomorph.2016.03.010.

Ryu, J.H., Won, J.S., Min, K.D., 2002. Waterline extraction from Landsat TM data in a tidal flat a case study in Gomso Bay, Korea. Remote Sens. Environ. 83, 442–456. https://doi.org/10.1016/S0034-4257(02)00059-7.

Ryu, J.H., Kim, C.H., Lee, Y.K., Won, J.S., Chun, S.S., Lee, S., 2008. Detecting the intertidal morphologic change using satellite data. Estuar. Coast. Shelf Sci. 78, 623–632. https://doi.org/10.1016/j.ecss.2008.01.020.

Salameh, E., Frappart, F., Marieu, V., Spodar, A., Parisot, J.P., Hanquiez, V., Turki, I., Laignel, B., 2018. Monitoring sea level and topography of coastal lagoons using satellite radar altimetry: the example of the Arcachon Bay in the Bay of Biscay. Remote Sens. 10, 1–22. https://doi.org/10.3390/rs10020297.

Salameh, E., Frappart, F., Almar, R., Baptista, P., Heygster, G., Lubac, B., Raucoules, D., Almeida, L.P., Bergsma, E.W.J., Capo, S., De Michele, M.D., Idier, D., Li, Z., Marieu, V., Poupardin, A., Silva, P.A., Turki, I., Laignel, B., 2019. Monitoring beach topography and nearshore bathymetry using spaceborne remote sensing: a review. Remote Sens. 11. https://doi.org/10.3390/rs11192212.

Shang, P., Shen, F., 2016. Atmospheric correction of satellite GF-1/WFV imagery and quantitative estimation of suspended particulate matter in the Yangtze estuary. Sensors. 16, 1997. https://doi.org/10.3390/s16121997.

Shen, F., Gao, A., Wu, J., Zhou, Y., Zhang, J., 2008. A Remotely sensed approach on waterline extraction of silty tidal flat for DEM construction, a case study in Jiuduansha Shoal of Yangtze River. Acta Geod. Cartogr. Sin. 37, 102–107.

Shen, F., Zhou, Y.X., Li, J.F., He, Q., Verhoef, W., 2013. Remotely sensed variability of the suspended sediment concentration and its response to decreased river discharge in the Yangtze estuary and adjacent coast. Cont. Shelf Res. 69, 52–61.

Si, Y., Ying, H., 2010. South Korea's first geostationary satellite launches successfully. Sp. Int. 7, 14–18.

Sun, N., Zhu, W., Cheng, Q., 2018. GF-1 and Landsat observed a 40-year wetland spatio-temporal variation and its coupled environmental factors in Yangtze River estuary. Estuar. Coast. Shelf Sci. 207, 30–39. https://doi.org/10.1016/j.ecss.2018.03.022.

Tan, K., Chen, J., Zhang, W., Liu, K., Tao, P., Cheng, X., 2020. Estimation of soil surface water contents for intertidal mudflats using a near-infrared long-range terrestrial laser scanner. ISPRS J. Photogramm. Remote Sens. 159, 129–139. https://doi.org/10.1016/j.isprsjprs.2019.11.003.

Tateishi, R., Akutsu, A., 1992. Relative DEM production from SPOT data without GCP. Int. J. Remote Sens. 13, 2517–2530. https://doi.org/10.1080/01431169208904061.

Tochamnanvit, T., Muttitanon, W., 2014. Investigation of coastline changes in three provinces of Thailand using remote sensing. Int. Arch. Photogramm. Remote. Sens. Spat. Inf. Sci. - ISPRS Arch. XL–8, 1079–1083. doi:https://doi.org/10.5194/isprsarchives-XL-8-1079-2014.

Wehr, A., Lohr, U., 1999. Airborne laser scanning - an introduction and overview. ISPRS J. Photogramm. Remote Sens. 54, 68–82. https://doi.org/10.1016/S0924-2716(99)00011-8.

Zhang, H., Li, Zhijia, Saifullah, M., Li, Q., Li, X., 2016. Impact of DEM resolution and spatial scale: analysis of influence factors and parameters on physically based distributed model, Adv. Meteorol. 10. https://doi.org/10.1155/2016/8582041.

Zhao, B., Guo, H., Yan, Y., Wang, Q., Li, B., 2008. A simple waterline approach for tidelands using multi-temporal satellite images: a case study in the Yangtze Delta. Estuar. Coast. Shelf Sci. 77, 134–142. https://doi.org/10.1016/j.ecss.2007.09.022.

Zhao, Q., Hou, G., Tang, Z., Shu, Z., 2018. Accuracy assessment of seven numerical models on simulating tides in the coastal area of Zhejiang. Adv. Mar. Sci. 36, 310–320.